Geophysical Research Letters

RESEARCH LETTER
10.1029/2023GL108012

Deep-Learning-Based Prediction of the Tetragonal → Cubic Transition in Davemaoite

Fulun Wu[1], Yang Sun[1,2], Tianqi Wan[2], Shunqing Wu[1], and Renata M. Wentzcovitch[2,3,4,5,6]

[1]Department of Physics, Xiamen University, Xiamen, China, [2]Department of Applied Physics and Applied Mathematics, Columbia University, New York, NY, USA, [3]Department of Earth and Environmental Sciences, Columbia University, New York, NY, USA, [4]Lamont–Doherty Earth Observatory, Columbia University, Palisades, NY, USA, [5]Data Science Institute, Columbia University, New York, NY, USA, [6]Center for Computational Quantum Physics, Flatiron Institute, New York, NY, USA

Abstract Davemaoite, that is, $CaSiO_3$ perovskite (CaPv), is the third most abundant phase in the lower mantle and exhibits a tetragonal-cubic phase transition at high pressures and temperatures. The phase boundary in CaPv has recently been proposed to be close to the cold slab adiabat and cause mid-mantle seismic wave speed anomalies (Thomson et al., 2019, https://doi.org/10.1038/s41586-019-1483-x). This study utilized accurate deep-learning-based simulations and thermodynamic integration techniques to compute free energies at temperatures ranging from 300 to 3,000 K and pressures up to 130 GPa. Our results indicate that CaPv exhibits a single cubic phase throughout lower-mantle conditions. This suggests that the phase diagram proposed by Thomson et al. requires revision, and mid-mantle seismic anomalies are likely attributable to other mechanisms.

Plain Language Summary Davemaoite, also known as calcium silicate perovskite (CaPv), is one of the most abundant minerals in Earth's lower mantle. It can exist in tetragonal and cubic crystal structures, depending on the pressure and temperature conditions. Determining the crystalline phase of CaPv is important for interpreting seismic observations of the lower mantle. A recent study (Thomson et al., 2019, https://doi.org/10.1038/s41586-019-1483-x) suggested that CaPv's tetragonal-to-cubic transition could cause mid-mantle seismic anomalies. However, this phase transition has been a topic of debate. Previous studies have attempted to determine the phase boundary using ab initio methods. The computational cost and challenges associated with handling strong anharmonicity limited these approaches' accuracy and predictive power. In this study, we utilized deep learning and thermodynamic integration techniques to accurately compute the tetragonal to cubic phase boundary of CaPv across the lower mantle pressure range. Our results satisfactorily explain previous experimental measurements and support the notion that CaPv remains in the cubic phase across lower mantle conditions. These findings challenge the previously proposed phase diagram by Thomson et al. and suggest that mid-mantle seismic scatterers/reflectors or large low-shear-velocity provinces in the lower mantle cannot be attributed to this transition in CaPv.

Key Points:

- A deep-learning potential is developed to accurately determine $CaSiO_3$ perovskite (CaPv)'s tetragonal-to-cubic phase boundary under lower-mantle conditions
- CaPv should exhibit solely a cubic phase throughout the entire lower mantle
- The tetragonal-to-cubic transition in CaPv is not a viable explanation for the mid-mantle seismic scatterers/reflectors or large low-shear-velocity provinces

Supporting Information:

Supporting Information may be found in the online version of this article.

Correspondence to:

Y. Sun, S. Wu and R. M. Wentzcovitch,
yangsun@xmu.edu.cn;
wsq@xmu.edu.cn;
rmw2150@columbia.edu

Citation:

Wu, F., Sun, Y., Wan, T., Wu, S., & Wentzcovitch, R. M. (2024). Deep-learning-based prediction of the tetragonal → cubic transition in davemaoite. *Geophysical Research Letters*, *51*, e2023GL108012. https://doi.org/10.1029/2023GL108012

Received 4 JAN 2024
Accepted 24 MAY 2024

Author Contributions:

Conceptualization: Yang Sun, Shunqing Wu
Data curation: Fulun Wu, Yang Sun
Formal analysis: Fulun Wu, Yang Sun, Tianqi Wan, Shunqing Wu, Renata M. Wentzcovitch
Funding acquisition: Yang Sun, Shunqing Wu, Renata M. Wentzcovitch
Investigation: Fulun Wu, Yang Sun, Tianqi Wan, Renata M. Wentzcovitch
Methodology: Fulun Wu, Yang Sun, Shunqing Wu

1. Introduction

$CaSiO_3$ perovskite (CaPv) is the third most abundant phase in a pyrolitic lower mantle and accounts for 24–29 vol% and 5–10 vol% of basaltic and pyrolitic assemblages, respectively (McDonough & Sun, 1995; Valencia-Cardona et al., 2017). Thermodynamic and thermoelastic properties of CaPv phases are crucial for a better understanding of Earth's interior, particularly for understanding potential compositional heterogeneities in the mantle and the D" region where basaltic compositions are expected to be abundant (Gréaux et al., 2019; Hirose et al., 2005; Kesson et al., 1994; Wang et al., 2020). Several experiments and theoretical studies have been carried out to unravel CaPv's structure and thermodynamic properties (Caracas et al., 2005; Komabayashi et al., 2007; Li et al., 2006; Prentice et al., 2019; Shim et al., 2002; Stixrude et al., 1996; Sun et al., 2014; Uchida et al., 2009; Zhang & Wentzcovitch, 2021). With increasing temperature, CaPv undergoes a tetragonal ($I4/mcm$) to cubic ($Pm\bar{3}m$) phase transition. Recent works have confirmed that cubic CaPv is stabilized by its strong anharmonic fluctuations at high temperatures (Prentice et al., 2019; Sun et al., 2014; Zhang & Wentzcovitch, 2021). Because tetragonal and cubic CaPv have rather different sound velocities (Gréaux et al., 2019; Thomson et al., 2019), their stability field under mantle conditions can be crucial to understanding velocity heterogeneities in the mantle if this transition occurs at mantle conditions.

Project administration: Yang Sun, Shunqing Wu, Renata M. Wentzcovitch
Resources: Yang Sun, Shunqing Wu
Software: Fulun Wu, Yang Sun, Tianqi Wan
Supervision: Yang Sun, Shunqing Wu, Renata M. Wentzcovitch
Validation: Fulun Wu, Yang Sun, Tianqi Wan
Visualization: Fulun Wu, Yang Sun
Writing – original draft: Fulun Wu
Writing – review & editing: Yang Sun, Tianqi Wan, Shunqing Wu, Renata M. Wentzcovitch

So far, the tetragonal-to-cubic phase boundary of CaPv under mantle pressures remains controversial. Stixrude et al. first predicted that the tetragonal-to-cubic CaPv transition occurs at temperatures above 2200 K and pressures of 80 GPa (Stixrude et al., 1996). However, Kurashina et al. conducted an experimental study and observed the phase transition at a much lower temperature of approximately 580 K and 50 GPa (Kurashina et al., 2004). It is important to note that the temperature measurements in Kurashina et al. had a significant uncertainty. Follow-up experiments conducted by Ono et al. (2004) and Murakami et al. (2005) using laser-heated DAC with synchrotron X-rays diffraction suggested the transition of CaPv to a cubic structure above 2000 K, while it maintained a tetragonal structure at room temperature. However, these studies did not provide precise phase boundaries at lower mantle conditions. In 2007, Komabayashi et al. performed X-ray diffraction experiments and determined that the transition temperature of CaPv ranged from 490 to 580 K at pressures between 27 and 72 GPa (Komabayashi et al., 2007), consistent with the findings of Ono et al. and Kurashina et al.. However, a study conducted in 2009 presented conflicting results, suggesting that CaPv remains a non-cubic phase up to 18 GPa and 1600 K (Uchida et al., 2009). Theoretical studies conducted by Adams using ab initio molecular dynamics in a metrically cubic supercell found the transition temperature to cubic CaPv to be between 1000 and 2000 K (Adams & Oganov, 2006). Similar conclusions were reached by Stixrude et al. using Landau mean-field potentials (Stixrude et al., 2007). However, Li et al. conducted AIMD and found that the hydrostatically compressed structure remained tetragonal up to 4000 K (Li et al., 2006). Sun et al. demonstrated that cubic CaPv is stabilized at approximately 600 K and 26 GPa (Sun et al., 2014). Overall, the experimental characterization of the phase boundary is challenging because cubic CaPv is not quenchable to ambient conditions (Komabayashi et al., 2007; Sun et al., 2014; Uchida et al., 2009). Ab initio calculations of the phase boundary of CaPv are also highly nontrivial due to strong anharmonicity in this system (Stixrude et al., 1996; Sun et al., 2014; Thomson et al., 2019). Free energy approaches, such as thermodynamic integration (TI) (Alfè et al., 2000) based on purely ab initio molecular dynamics (AIMD) can be used but is computationally intensive, thus only practical for small systems.

In 2019, Thomson et al. observed the tetragonal-to-cubic phase transition in CaPv at ∼12 GPa through in situ diffraction and identified the reduction of the seismic velocity along with the phase transition (Thomson et al., 2019). To understand the geophysical consequence of this transition, they combined the experimental measurement and ab initio calculations to determine the phase boundary of CaPv at lower mantle pressures. The slope of the CaPv phase boundary was estimated by ab initio free energy calculations as dT/dP ∼15 K/GPa. Using the calculated dT/dP, they extrapolated the experimental data from 12 GPa to the entire lower mantle pressures and found the CaPv undergoes a cubic–tetragonal transition in cold slab assemblages at pressures greater than 90 GPa. Their phase boundary thus was proposed to explain the seismic anomalies in the mantle, such as the mid-mantle reflectors and large low-shear-velocity provinces (LLSVPs) in the deep mantle (Thomson et al., 2019). However, their theoretical slope of the phase boundary was obtained via an approximated thermodynamic integration method and the data deviated significantly from Komabayashi et al.'s experimental value of ∼1.1 ± 1.3 K/GPa (Komabayashi et al., 2007).

Considering the lack of consensus between these studies, it is evident that further investigations are required to gain a deeper understanding of the phase transition in CaPv, though purely ab initio calculations remain challenging. Recently, interatomic potentials developed with machine learning techniques such as Neural Network Potential (NNP) (Behler & Parrinello, 2007), Gaussian Approximation Potential (GAP) (Bartók et al., 2010), on-the-fly Machine Learning Force Field (MLFF) (Jinnouchi et al., 2019), and Deep Potential for Molecular Dynamics (DPMD) (Zhang, Han, Wang, Saidi, et al., 2018) have significantly extended the timescale and length scale of ab initio simulation. These algorithms can incorporate large amounts of computational or experimental data to construct direct mappings from atomic structures to forces and energies, thus saving significant amounts of computational time required for ab initio calculations (Bartók et al., 2010; Behler, 2016; Behler & Parrinello, 2007; Chmiela et al., 2017; Huan et al., 2017; Liu et al., 2023; Morawietz et al., 2016; Rupp et al., 2012; Schütt et al., 2017; Smith et al., 2017; Thompson et al., 2015). Particularly, the DP method has recently shown its ability to capture higher-order anharmonic force constant (Yang et al., 2022), which can be useful in studying the high-temperature properties of strongly anharmonic materials. By combining with molecular dynamics, DP has proven to be effective in the study of several systems under high-PT conditions, for example, $MgSiO_3$ (Deng et al., 2023; Luo et al., 2021; Wan et al., 2023; Yang et al., 2022), FeSiO melts (Tang et al., 2023; Zhang et al., 2022), δ-AlOOH (Luo et al., 2023), dense lithium (Wang et al., 2023), high-pressure phases of tin (Chen et al., 2023), solid and fluid H_2O (Zhang et al., 2021) etc.

In this work, we use the DP method to study phase transitions in CaPv at temperatures ranging from 300 to 3000K and pressures up to 130 GPa. We develop DP potentials with an active learning method and demonstrate its accuracy in predicting energies, forces, and vibrational properties at various PT conditions. By combining the DP and the TI methods, we compute the phase boundary between the tetragonal and cubic phases of CaPv throughout the lower mantle's pressure range and discuss its implication on the seismic anomaly in the lower mantle.

2. Methods

2.1. First-Principles Calculations

Ab initio calculations were performed using the Vienna Ab-initio Simulation Package (VASP) (Kresse & Furthmüller, 1996; Kresse & Hafner, 1993), which implements the projector-augmented wave (PAW) (Blöchl, 1994; Perdew et al., 1996) methodology of density functional theory. Functionals with the local density approximations (LDA) (Perdew & Zunger, 1981) and the generalized gradient approximation (GGA) (Perdew et al., 1996) were studied. PAW potentials with valence electronic configurations $3s^2 3p^6 4s^2$, $3s^2 3p^2$, and $2s^2 2p^4$ for Ca, Si, and O were used. A plane wave energy cutoff of 550 eV and a $2 \times 2 \times 2$ k-point grid for the 40-atom supercell were used, which was shown to be sufficient to achieve convergence in calculating anharmonic phonon dispersions (Zhang & Wentzcovitch, 2021). Two independent DP models, using LDA and GGA data sets, were developed and are referred to as DP-LDA and DP-GGA, respectively. The smooth edition descriptor *se_e2_a* proposed by Zhang et al. (Zhang, Han, Wang, Car, & E, 2018; Zhang, Han, Wang, Saidi, et al., 2018) was employed to train these models (see training details in Text S1 in Supporting Information S1).

2.2. Phonon Calculations

The harmonic phonon spectrum was calculated using the finite displacement supercell approach implemented in the Phonopy (Togo & Tanaka, 2015). Anharmonic effects were addressed by the phonon quasiparticle method (Zhang et al., 2019). Temperature-dependent anharmonic phonon dispersions were computed by projecting the atomic velocities onto the harmonic phonon eigenvectors of the temperature-dependent equilibrium structure. In this method, the phonon frequencies and corresponding linewidths can be extracted directly from the MD trajectories, as described by Sun et al. (2014). The DP-based molecular dynamics (DPMD) simulations were used to obtain the mode-projected velocity auto-correlation functions (VAF) (Zhang et al., 2014). The simulations were performed using the NVT ensemble and ran for over 60 ps with the time step of 1 fs and a supercell consisting of 40 atoms.

2.3. Thermodynamic Integration Calculation

To calculate the free energies of the $I4/mcm$ and $Pm\bar{3}m$ phases of CaPv, we used a state-of-the-art TI method developed by Freitas et al. (2016). It provides an efficient method to sample the full TI path from the reference state and target state. Using DPMD simulations, we numerically integrated the work from an initial equilibrium state to the final equilibrium state of interest. At a specific (P_0,T_0) condition, the Gibbs free energy of CaPv is

$$G_{\mathrm{CaPv}}(P_0,T_0) = F_{\mathrm{CaPv}}(V_0,T_0) + P_0V_0, \tag{1}$$

where V_0 is the volume at (P_0,T_0), which can be obtained from the equation of state (EOS) of CaPv phases calculated from the NVT (constant number of atoms, volume, and temperature ensemble) MD simulations, shown in Figure 2 and Figure S3 in Supporting Information S1. The Helmholtz free energy F_{CaPv} at (V_0,T_0) condition is calculated via TI method through the NVT-MD simulations, as

$$F_{\mathrm{CaPv}}(V_0,T_0) = F_E(V_0,T_0) + \Delta F(V_0,T_0), \tag{2}$$

where $F_E(V_0,T_0)$ represents the Helmholtz free energy of Einstein reference crystal at (V_0, T_0) and $\Delta F(V_0,T_0)$ is the Helmholtz free energy difference at (V_0,T_0). The Hamiltonian of the Einstein reference crystal is:

$$H_E = \sum_{i=1}^{N}\left[\frac{\boldsymbol{p}_i^2}{2m} + \frac{1}{2}m\omega^2\left(\boldsymbol{r}_i - \boldsymbol{r}_i^0\right)^2\right], \tag{3}$$

where ω is the oscillator frequency and $\boldsymbol{r}_i^0$ is the equilibrium position of particle i. Its Helmholtz free energy at (V_0, T_0) is given by

$$F_E(V_0,T_0) = 3k_B T_0 \ln\left(\frac{\hbar\omega}{k_B T}\right). \quad (4)$$

To closely match the characteristic vibrational spectrum of the CaPv system, the value of ω was obtained through NVT-MD simulations at (V_0,T_0) conditions. The mean-squared displacement $<(\Delta r)^2>$ of atoms in the CaPv system was used to determine ω based on the equipartition theorem as $m\omega^2 = \frac{3k_B T}{<(\Delta r)^2>}$ (Freitas et al., 2016). This approach differs from the method employed in Thomson et al. (2019), where ω was obtained using harmonic force constants with the artificial elimination of imaginary phonon modes. Since our MD simulations already incorporate the effects of anharmonicity, the determination of ω using the mean square displacement (MSD) method introduced by Freitas et al. (2016) provides a more realistic reference state. The TI method (Freitas et al., 2016) provides a continuous path from the Einstein crystal to CaPv. The forward and backward integration processes were employed to enhance the sampling of the transition pathway. The free energy difference $\Delta F(V_0$, $T_0)$ was computed by NVT-MD simulation at (V_0,T_0) condition, as

$$\Delta F = \frac{1}{2}\left(W^{irr}_{\text{Ein}\to\text{CaPv}} - W^{irr}_{\text{CaPv}\to\text{Ein}}\right), \quad (5)$$

where $W^{irr}_{\text{Ein}\to\text{CaPv}}$ is the irreversible work to transform the Hamiltonian from the Einstein crystal to CaPv, which is noted as

$$W^{irr}_{\text{Ein}\to\text{CaPv}} = \int_0^1 \langle U_{CaPv} - U_{Ein}\rangle_\lambda \, d\lambda, \quad (6)$$

where U_{Ein} and U_{CaPv} are the potential energies for the Einstein crystal and CaPv, respectively. λ is the coupling parameter between the Einstein crystal and CaPv, which generates a new potential energy function in TI as $U = \lambda U_{CaPv} + (1-\lambda)U_{Ein}$. The "forward" and "backward" terms refer to the direction in which the thermodynamic parameter λ is varied during the switching process. The "forward" process (noted as Ein → CaPv) refers to varying the parameter λ from an initial value $\lambda = 0$ (Einstein crystal) to a final value $\lambda = 1$ (CaPv), while the "backward" process (CaPv → Ein) refers to the reverse. Averaging the work from the forward and backward processes in Equation 5 eliminates systematic errors arising from irreversible work dissipation during the nonequilibrium switching. During this continuous switching process, the parameter λ varies smoothly from 0 to 1 in 100,000 TI-MD steps. A supercell of 2,560 atoms was used to compute the $\Delta F(V_0,T_0)$ for both tetragonal and cubic phases of CaPv. We noted that at the transition temperatures, the tetragonal phase is metastable and its c/a remains unchanged in the MD simulations.

3. Results and Discussion

3.1. Phonon Dispersion and Equation of States

We collected 3,420 unique configurations that capture a variety of local atomic environments from the ab initio data exploration across temperature ranges of 300 to 3,000 K and pressure ranges of 20–130 GPa (see more details in the Text S1 in Supporting Information S1). We split the data set into 80% for training and 20% for validation. To evaluate the accuracy of the DP, the root mean square errors (RMSEs) of energies, atomic forces, and pressures were compared to DFT calculations for the CaPv system. The results, as shown in Figures S1a–S1c in Supporting Information S1, suggest excellent agreement between DP and DFT calculations, with RMSEs of about 2.0 meV/atom for energies, 0.052 eV/Å for forces and 0.2 GPa for pressures. Similar accuracy was also achieved for DP-GGA, as shown in Figures S1d–S1f in Supporting Information S1. The RMSEs of the training and validating sets are similar, suggesting the neural network was not overfitting. Furthermore, the wide energy distribution displayed in Figures S1a and S1d in Supporting Information S1 indicates the complexity of the configuration spaces involved in exploring the potential energy surface.

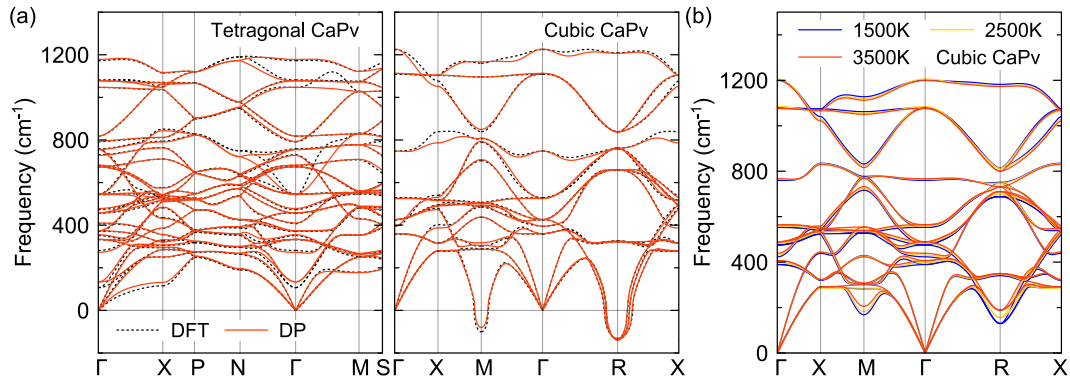

Figure 1. (a) Harmonic phonon dispersions of tetragonal and cubic CaPv at 70 GPa and 0K along high-symmetry lines in the Brillouin zone by DP and DFT with LDA functional. (c) Anharmonic phonon dispersions of cubic CaPv at temperatures of 1500, 2500, and 3500K by DP.

The sensitivity of the phonon dispersion relations to the accuracy of atomic interactions stems from their dependence on the quality of the force constant matrix (dynamical or Hessian matrix). The DP potentials were then applied to determine the interatomic force constants and dynamical matrices via the finite displacement method (Togo & Tanaka, 2015). Figure 1 demonstrates that the DP potential accurately reproduces the harmonic phonon spectra for both tetragonal and cubic CaPv phases. It is noteworthy that the DP method accurately reproduces the soft phonon modes at $\boldsymbol{M}$(1/2, 1/2, 0) and $\boldsymbol{R}$(1/2,1/2,1/2) in cubic CaPv at 0 K, as shown in Figure 1a. Similar results are also found for DP-PBE potentials, shown in Figure S2 in Supporting Information S1. While soft and unstable modes are present at 0 K in the cubic phase, they can be stabilized at higher temperatures by anharmonic effects (Sun et al., 2014). The temperature-dependent phonon dispersions at 1500, 2500, and 3500K were then calculated using the phonon quasiparticle method (Zhang et al., 2019) with the DP model. As shown in Figure 1b, while most phonon modes showed a weak temperature dependence, significant frequency renormalization was observed at $\boldsymbol{M}$(1/2, 1/2, 0) and $\boldsymbol{R}$(1/2,1/2,1/2) as the temperature increased, due to strong lattice anharmonicity. In comparison to the harmonic phonon spectrum for cubic CaPv in Figure 1a, the imaginary frequencies at $\boldsymbol{M}$ and $\boldsymbol{R}$ were lifted to positive frequencies, indicating the dynamic stability of the structure. This reproduces the LDA results in Zhang et al. (Zhang & Wentzcovitch, 2021). Similar frequency renormalization is also found with the DP-GGA. The accurate prediction of the anharmonic phonon dispersions demonstrates the ability of our DP to describe both the harmonic lattice dynamics and high-temperature effect, which is crucial for accurately capturing the phase transitions.

We further compare the equation of state (EOS) of CaPv with previous results to validate DP potential across a wide range of *P-T* conditions. Figures 2a and 2b show that the EOSs of cubic CaPv from our DP-LDA and DP-GGA agree well with previous DFT calculations (Kawai & Tsuchiya, 2014; Li et al., 2006; Sagatova et al., 2021) at 300 and 2000 K. The experimental EOS data (Chen et al., 2018; Gréaux et al., 2019; Mao et al., 1989; Ricolleau et al., 2010; Shim et al., 2002; Sun et al., 2016; Thomson et al., 2019; Wang et al., 1996) are mostly between the LDA and GGA results. It is expected because the GGA functional often overestimates the equilibrium volume, while the LDA almost invariably underestimates it. We note that the difference in EOS between the tetragonal and cubic phases of CaPv is very small, as shown in Figure S3 in Supporting Information S1.

3.2. Phase Transition of CaPv

To describe the relative stability between the tetragonal and cubic phases of CaPv, we compute their Gibbs free energy difference $\Delta G(T,p) = G_{tet}(T,P) - G_{cub}(T,P)$ at different *P-T* conditions. A negative ΔG indicates that the tetragonal phase is more favorable and vice versa. We employ the TI method to compute the G_{tet} and G_{cub} for tetragonal and cubic phases, respectively. The DP-based TI-MD was performed at different temperatures and pressures for the two phases. The energy differences between the CaPv and Einstein crystal reference, denoted as $\Delta U(\lambda) = \langle U_{\mathrm{CaPv}} - U_{ref} \rangle$, were obtained from TI-MD. As shown in Figure 3, the transition paths from the Einstein crystal ($\lambda = 0$) to the CaPv ($\lambda = 1$) were smooth for both tetragonal and cubic phases. The highly nonlinear transition path suggests a significant difference between the two systems. Therefore, one must sample this transition path with a continuously changing λ, which is achieved by the present TI method. Previous studies

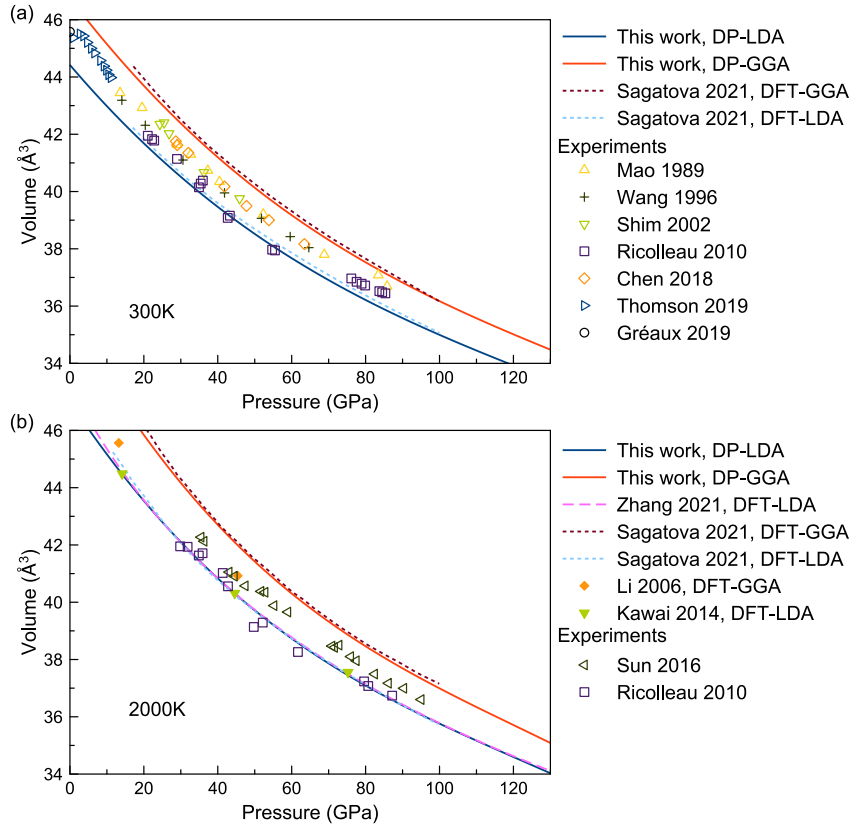

Figure 2. Equation of state of cubic CaPv at (a) 300 K and (b) 2000 K. Solid curves are obtained using DP, and dashed lines are the DFT results (Kawai & Tsuchiya, 2014; Li et al., 2006; Sagatova et al., 2021; Zhang & Wentzcovitch, 2021), and experimental data are taken from Refs.(Chen et al., 2018; Gréaux et al., 2019; Mao et al., 1989; Ricolleau et al., 2010; Shim et al., 2002; Sun et al., 2016; Thomson et al., 2019; Wang et al., 1996).

suggested the size effect can be significant in TI (Sun et al., 2023). To examine this effect, we conducted the TI simulations with different numbers of atoms for both phases in Figure 4a. It shows a simulation size larger than 2,000 atoms can converge the free energy calculation within 0.1 meV/atom. The source of errors in the simulation is discussed in the Text S2 in Supporting Information S1.

We show $\Delta G(T)$ with DP-LDA at 50 GPa in Figure 4b. More $\Delta G(T)$ results at various pressure are shown in the Figure S4 in Supporting Information S1. The tetragonal-cubic phase transition temperatures T_c were obtained from the conditions where $\Delta G(T_c) = 0$. For DP-LDA, the phase boundary exists around 415 K at 25 GPa, 510 K at

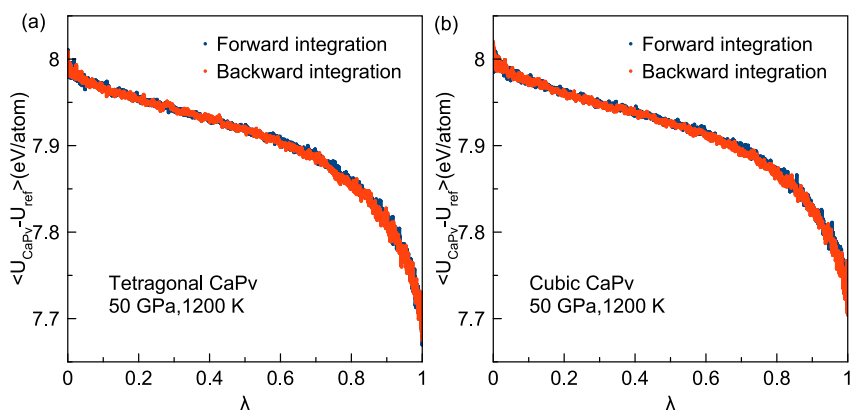

Figure 3. TI calculations at 50 GPa and 1200K. Panels (a–b) show the averaged energy differences between the final system ($\lambda = 1$) and reference system ($\lambda = 0$) in TI-MD simulations for tetragonal and cubic CaPv, respectively.

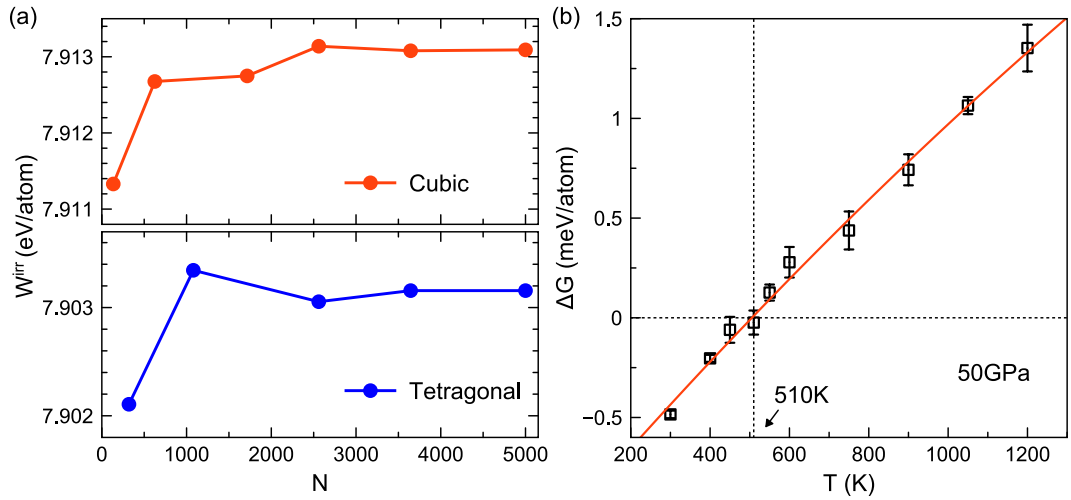

Figure 4. (a) Size effect on the irreversible work with DP-based TI simulations. The circles are W^{irr} measured from the TI with different numbers of atoms, N, in the simulations at 50 GPa and 1200 K. (b) The Gibbs free energy difference between the tetragonal and cubic phase for the CaPv at 50 GPa (See Figure S2 in Supporting Information S1 for more pressures). Negative energy difference indicates that the tetragonal phase is more favorable, and vice versa.

50 GPa, 670 K at 75 GPa, 930 K at 100 GPa, and 1240 K at 125 GPa. We also computed $\Delta G(T)$ with DP-GGA in Figure S5 in Supporting Information S1. For DP-GGA, the phase boundary is around 270 K at 25 GPa, 365 K at 50 GPa, 515K at 75 GPa, 680 K at 100 GPa, and 875 K at 125 GPa. It is worth mentioning that even if the most advanced massively parallel computers are employed, carrying out these simulations using full ab initio calculations is prohibitively time-consuming. With the DP-LDA, we also performed a cooling simulation on cubic CaPv at 125 GPa. As shown in Figure S6 in Supporting Information S1, the cubic phase transformed into the tetragonal phase in the range of 1200–1400 K, consistent with the phase boundary obtained from the free energy calculations.

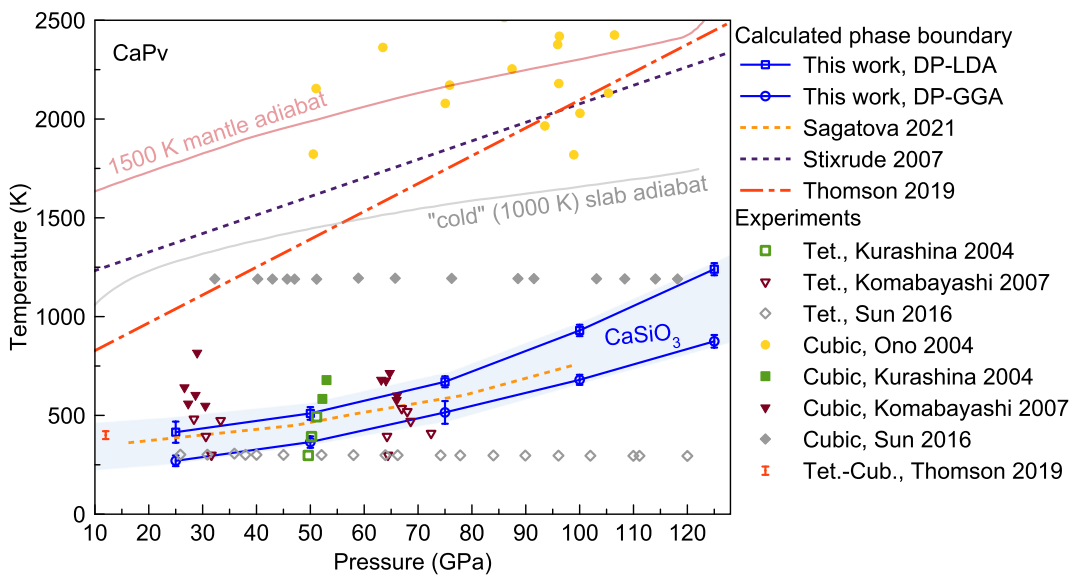

Figure 5. Phase diagram of Ca-perovskite across the mantle pressure range. Previous data includes calculations by Sagatova et al. (2021), Stixrude et al. (2007), Thomson et al. (2019) and experiments by Komabayashi et al. (2007), Kurashina et al. (2004), Ono et al. (2004), Sun et al. (2016), and Thomson et al. (2019). The shaded blue area indicates the uncertainty due to the DFT functional. The brown and gray solid lines depict 1,500 K mantle adiabat and 1,000 K "cold" slab temperature profiles, respectively.

Figure 5 shows the tetragonal-cubic phase boundary of CaPv obtained from our DP calculations. The DP-LDA results in a higher transition temperature than the DP-GGA by 200–500K. The differences increase with increasing pressure. The tendency of GGA to predict the phase-transition pressure higher than LDA for CaPv is similar to that demonstrated in many other phase-transition studies (Jaffe et al., 2000; Tsuchiya et al., 2004; Yu et al., 2011). Such a tendency can be attributed to the different dependence of the exchange-correlation functional on the electron density in LDA and GGA. Nevertheless, both phase boundaries from LDA and GGA calculations are significantly lower than the earlier calculations from Stixrude et al. (2007) and Thomson et al. (2019) by more than 1000 K at lower mantle pressures. The high computational cost of fully ab initio calculations has forced these studies to rely on approximated free energy calculations. Stixrude et al. (2007) used a Landau potential that relies on a few empirical parameters to fit the ab initio data. This model may not be sufficiently accurate to describe the vanishing free energy difference between the cubic and tetragonal phases near the true critical point. Thomson et al. (2019) used a perturbation method to apply a first-order approximation on the TI as the energy difference between the reference state and CaPv, as $F - F_0 \cong \langle U - U_0 \rangle_0 + \frac{1}{2k_B T} \left\langle \left[U - U_0 - \langle U - U_0 \rangle_0 \right]^2 \right\rangle_0$. The accuracy of this equation highly depends on the linearity of the TI path. However, as shown in Figure 3, the TI path from the reference state to CaPv is highly nonlinear, so such an approximation is inaccurate for the CaPv system. Sagatova's DFT result (Sagatova et al., 2021) is similar to ours, where a self-consistent phonon algorithm (SCPH) (Tadano et al., 2014; Tadano & Tsuneyuki, 2015) was used to perform anharmonic phonon calculations.

The difference between LDA and GGA functionals can be treated as the computational uncertainty of the present calculated phase boundary, which provides upper and lower bounds. We consider this region as the confident interval of our calculations due to DFT functionals (blue region in Figure 5). Compared to experimental data, our phase boundary is consistent with all previous measurements (Komabayashi et al., 2007; Kurashina et al., 2004; Ono et al., 2004), including Thomson et al.'s experimental results at 12 GPa (Thomson et al., 2019). The dT/dP slope is ∼7 K/GPa, significantly smaller than the calculated results in Thomson et al. (2019).

Our tetragonal-to-cubic boundaries of CaPv lie well below the cold slab geotherm (Shim et al., 2002), where CaPv is supposed to be abundant, or any adiabatic mantle geotherm, suggesting that CaPv should be cubic in all lower mantle environments. Therefore, the tetragonal to cubic transition in CaPv cannot explain the seismic wave speed anomalies in the lower mantle, contrary to the claim of Thomson et al. (2019). The mid-mantle reflectors or scatters may be caused by other mechanisms, for example, the post-stishovite phase transition in pure or aluminous-hydrous silica (Umemoto et al., 2016; Wang et al., 2020) in stagnant subducted slabs (Zhang et al., 2023). Recently, Ko et al. suggested that the dissolution behavior of CaPv in bridgmanite can lead to its disappearance as a separate phase at depths greater than 1,800 km, a new insight into the deep mantle mineralogy (Ko et al., 2022). Irrespective of this dissolution behavior, the problem addressed here is relevant for addressing the origin of seismic scatterers above 1800 km depth.

4. Conclusion

We have implemented DP models for $CaSiO_3$ perovskite using both LDA and GGA functionals. The simulations with the DP model reproduce the harmonic and anharmonic phonon dispersions from DFT calculations. The comparison with experiments suggests that volume versus pressure in EOS is underestimated by the LDA and overestimated by the GGA functionals. Overall, the machine learning approach can describe the strongly anharmonic properties of CaPv with ab initio accuracy. Based on the DP model, we employ the TI method to fully sample the transition path from the reference state of a harmonic crystal to the CaPv phases. The transition path shows strong nonlinearity w.r.t. the integration parameter λ which suggests that TI in this system cannot be approximated as the energy difference between the initial and final states. Therefore, the previously calculated phase boundary in Thomson et al. (2019) is questionable. With the present DP model and TI method, we provide accurate free energy difference between the cubic and tetragonal phases in a large pressure and temperature range close to lower mantle conditions. We determined the tetragonal-to-cubic transition temperatures versus pressure in CaPv and computed the thermodynamic phase boundary. We can satisfactorily explain previous experimental measurements. Based on our phase boundary, the CaPv are cubic at lower mantle conditions. It suggests that the observed seismic velocity anomalies in the mid-mantle and in LLSVPs cannot be explained by the tetragonal-to-cubic phase transition in CaPv and is likely attributable to other mechanisms.

Data Availability Statement

The authors comply with the AGU's data policy, and the data sets of this paper are available at Zenodo (F. Wu, 2024).

Acknowledgments
We are grateful to Rodrigo Freitas for the help on the thermodynamic integration method. Work at Xiamen University was supported by National Natural Science Foundation of China (Grants 12374015 and 42374108). Work at Columbia University was supported by NSF (Grants EAR-2000850 and EAR-1918126). Work at Iowa State University was supported by NSF Grant EAR-1918134. Shaorong Fang and Tianfu Wu from the Information and Network Center of Xiamen University are acknowledged for their help with the Graphics Processing Unit (GPU) computing. The supercomputing was supported by the Opening Project of the Joint Laboratory for Planetary Science and Supercomputing (no. CSYYGS-QT-2024-15), Research Center for Planetary Science, and the National Supercomputing Center in Chengdu.

References

Adams, D. J., & Oganov, A. R. (2006). Ab initio molecular dynamics study of $CaSiO_3$ perovskite at P-T conditions of Earth's lower mantle. *Physical Review B: Condensed Matter*, *73*(18), 184106. https://doi.org/10.1103/PhysRevB.73.184106

Alfè, D., de Wijs, G. A., Kresse, G., & Gillan, M. J. (2000). Recent developments in ab initio thermodynamics. *International Journal of Quantum Chemistry*, *77*(5), 871–879. https://doi.org/10.1002/(SICI)1097-461X(2000)77:5<871::AID-QUA8>3.0.CO;2-3

Bartók, A. P., Payne, M. C., Kondor, R., & Csányi, G. (2010). Gaussian approximation potentials: The accuracy of quantum mechanics, without the electrons. *Physical Review Letters*, *104*(13), 136403. https://doi.org/10.1103/PhysRevLett.104.136403

Behler, J. (2016). Perspective: Machine learning potentials for atomistic simulations. *Journal of Chemical Physics*, *145*(17), 170901. https://doi.org/10.1063/1.4966192

Behler, J., & Parrinello, M. (2007). Generalized neural-network representation of high-dimensional potential-energy surfaces. *Physical Review Letters*, *98*(14), 146401. https://doi.org/10.1103/PhysRevLett.98.146401

Blöchl, P. E. (1994). Projector augmented-wave method. *Physical Review B: Condensed Matter*, *50*(24), 17953–17979. https://doi.org/10.1103/PhysRevB.50.17953

Caracas, R., Wentzcovitch, R., Price, G. D., & Brodholt, J. (2005). $CaSiO_3$ perovskite at lower mantle pressures. *Geophysical Research Letters*, *32*(6). https://doi.org/10.1029/2004GL022144

Chen, H., Shim, S.-H., Leinenweber, K., Prakapenka, V., Meng, Y., & Prescher, C. (2018). Crystal structure of CaSiO3 perovskite at 28–62 GPa and 300 K under quasi-hydrostatic stress conditions. *American Mineralogist*, *103*(3), 462–468. https://doi.org/10.2138/am-2018-6087

Chen, T., Yuan, F., Liu, J., Geng, H., Zhang, L., Wang, H., & Chen, M. (2023). Modeling the high-pressure solid and liquid phases of tin from deep potentials with ab initio accuracy. *Physical Review Materials*, *7*(5), 053603. https://doi.org/10.1103/PhysRevMaterials.7.053603

Chmiela, S., Tkatchenko, A., Sauceda, H. E., Poltavsky, I., Schütt, K. T., & Müller, K.-R. (2017). Machine learning of accurate energy-conserving molecular force fields. *Science Advances*, *3*(5), e1603015. https://doi.org/10.1126/sciadv.1603015

Deng, J., Niu, H., Hu, J., Chen, M., & Stixrude, L. (2023). Melting of $MgSiO_3$ determined by machine learning potentials. *Physical Review B: Condensed Matter*, *107*(6), 064103. https://doi.org/10.1103/PhysRevB.107.064103

Freitas, R., Asta, M., & De Koning, M. (2016). Nonequilibrium free-energy calculation of solids using LAMMPS. *Computational Materials Science*, *112*, 333–341. https://doi.org/10.1016/j.commatsci.2015.10.050

Gréaux, S., Irifune, T., Higo, Y., Tange, Y., Arimoto, T., Liu, Z., & Yamada, A. (2019). Sound velocity of CaSiO3 perovskite suggests the presence of basaltic crust in the Earth's lower mantle. *Nature*, *565*(7738), 218–221. https://doi.org/10.1038/s41586-018-0816-5

Hirose, K., Takafuji, N., Sata, N., & Ohishi, Y. (2005). Phase transition and density of subducted MORB crust in the lower mantle. *Earth and Planetary Science Letters*, *237*(1–2), 239–251. https://doi.org/10.1016/j.epsl.2005.06.035

Huan, T. D., Batra, R., Chapman, J., Krishnan, S., Chen, L., & Ramprasad, R. (2017). A universal strategy for the creation of machine learning-based atomistic force fields. *Npj Computational Materials*, *3*(1), 37. https://doi.org/10.1038/s41524-017-0042-y

Jaffe, J. E., Snyder, J. A., Lin, Z., & Hess, A. C. (2000). LDA and GGA calculations for high-pressure phase transitions in ZnO and MgO. *Physical Review B: Condensed Matter*, *62*(3), 1660–1665. https://doi.org/10.1103/PhysRevB.62.1660

Jinnouchi, R., Karsai, F., & Kresse, G. (2019). On-the-fly machine learning force field generation: Application to melting points. *Physical Review B: Condensed Matter*, *100*(1), 014105. https://doi.org/10.1103/PhysRevB.100.014105

Kawai, K., & Tsuchiya, T. (2014). P-V-T equation of state of cubic $CaSiO_3$ perovskite from first-principles computation. *Journal of Geophysical Research: Solid Earth*, *119*(4), 2801–2809. https://doi.org/10.1002/2013JB010905

Kesson, S. E., Fitz Gerald, J. D., & Shelley, J. M. G. (1994). Mineral chemistry and density of subducted basaltic crust at lower-mantle pressures. *Nature*, *372*(6508), 767–769. https://doi.org/10.1038/372767a0

Ko, B., Greenberg, E., Prakapenka, V., Alp, E. E., Bi, W., Meng, Y., et al. (2022). Calcium dissolution in bridgmanite in the Earth's deep mantle. *Nature*, *611*(7934), 88–92. https://doi.org/10.1038/s41586-022-05237-4

Komabayashi, T., Hirose, K., Sata, N., Ohishi, Y., & Dubrovinsky, L. S. (2007). Phase transition in CaSiO3 perovskite. *Earth and Planetary Science Letters*, *260*(3–4), 564–569. https://doi.org/10.1016/j.epsl.2007.06.015

Kresse, G., & Furthmüller, J. (1996). Efficient iterative schemes for ab initio total-energy calculations using a plane-wave basis set. *Physical Review B: Condensed Matter*, *54*(16), 11169–11186. https://doi.org/10.1103/PhysRevB.54.11169

Kresse, G., & Hafner, J. (1993). Ab initio molecular dynamics for liquid metals. *Physical Review B: Condensed Matter*, *47*(1), 558–561. https://doi.org/10.1103/PhysRevB.47.558

Kurashina, T., Hirose, K., Ono, S., Sata, N., & Ohishi, Y. (2004). Phase transition in Al-bearing CaSiO3 perovskite: Implications for seismic discontinuities in the lower mantle. *Physics of the Earth and Planetary Interiors*, *145*(1–4), 67–74. https://doi.org/10.1016/j.pepi.2004.02.005

Li, L., Weidner, D. J., Brodholt, J., Alfè, D., Price, G. D., Caracas, R., & Wentzcovitch, R. (2006). Phase stability of CaSiO3 perovskite at high pressure and temperature: Insights from ab initio molecular dynamics. *Physics of the Earth and Planetary Interiors*, *155*(3–4), 260–268. https://doi.org/10.1016/j.pepi.2005.12.007

Liu, J., Sun, Y., Lv, C., Zhang, F., Fu, S., Prakapenka, V. B., et al. (2023). Iron-rich Fe–O compounds at Earth's core pressures. *The Innovation*, *4*(1), 100354. https://doi.org/10.1016/j.xinn.2022.100354

Luo, C., Sun, Y., & Wentzcovitch, R. M. (2023). High throughput sampling of phase space with deep learning potentials: δ-AlOOH at geophysical conditions. https://doi.org/10.48550/arXiv.2309.06712

Luo, H., Karki, B. B., Ghosh, D. B., & Bao, H. (2021). Anomalous Behavior of viscosity and electrical conductivity of $MgSiO_3$ melt at mantle conditions. *Geophysical Research Letters*, *48*(13), e2021GL093573. https://doi.org/10.1029/2021GL093573

Mao, H. K., Chen, L. C., Hemley, R. J., Jephcoat, A. P., Wu, Y., & Bassett, W. A. (1989). Stability and equation of state of CaSiO3-Perovskite to 134 GPa. *Journal of Geophysical Research*, *94*(B12), 17889–17894. https://doi.org/10.1029/JB094iB12p17889

McDonough, W. F., & Sun, S.-s. (1995). The composition of the Earth. *Chem. Geol., Chemical Evolution of the Mantle*, *120*(3–4), 223–253. https://doi.org/10.1016/0009-2541(94)00140-4

Morawietz, T., Singraber, A., Dellago, C., & Behler, J. (2016). How van der Waals interactions determine the unique properties of water. *Proceedings of the National Academy of Sciences*, *113*(30), 8368–8373. https://doi.org/10.1073/pnas.1602375113

Murakami, M., Hirose, K., Sata, N., & Ohishi, Y. (2005). Post-perovskite phase transition and mineral chemistry in the pyrolitic lowermost mantle. *Geophysical Research Letters*, *32*(3), L03304. https://doi.org/10.1029/2004GL021956

Ono, S., Ohishi, Y., & Mibe, K. (2004). Phase transition of Ca-perovskite and stability of Al-bearing Mg-perovskite in the lower mantle. *American Mineralogist*, *89*(10), 1480–1485. https://doi.org/10.2138/am-2004-1016

Perdew, J. P., Burke, K., & Ernzerhof, M. (1996). Generalized gradient approximation made simple. *Physical Review Letters*, *77*(18), 3865–3868. https://doi.org/10.1103/PhysRevLett.77.3865

Perdew, J. P., & Zunger, A. (1981). Self-interaction correction to density-functional approximations for many-electron systems. *Physical Review B: Condensed Matter*, *23*(10), 5048–5079. https://doi.org/10.1103/PhysRevB.23.5048

Prentice, J. C. A., Maezono, R., & Needs, R. J. (2019). First-principles anharmonic vibrational study of the structure of calcium silicate perovskite under lower mantle conditions. *Physical Review B: Condensed Matter*, *99*(6), 064101. https://doi.org/10.1103/PhysRevB.99.064101

Ricolleau, A., Perrillat, J.-P., Fiquet, G., Daniel, I., Matas, J., Addad, A., et al. (2010). Phase relations and equation of state of a natural MORB: Implications for the density profile of subducted oceanic crust in the Earth's lower mantle. *Journal of Geophysical Research*, *115*(B8), B08202. https://doi.org/10.1029/2009JB006709

Rupp, M., Tkatchenko, A., Müller, K.-R., & von Lilienfeld, O. A. (2012). Fast and Accurate modeling of molecular atomization energies with machine learning. *Physical Review Letters*, *108*(5), 058301. https://doi.org/10.1103/PhysRevLett.108.058301

Sagatova, D. N., Shatskiy, A. F., Sagatov, N. E., & Litasov, K. D. (2021). Phase relations in $CaSiO_3$ system up to 100 GPa and 2500 K. *Geochemistry International*, *59*(8), 791–800. https://doi.org/10.1134/S0016702921080073

Schütt, K. T., Arbabzadah, F., Chmiela, S., Müller, K. R., & Tkatchenko, A. (2017). Quantum-chemical insights from deep tensor neural networks. *Nature Communications*, *8*(1), 13890. https://doi.org/10.1038/ncomms13890

Shim, S.-H., Jeanloz, R., & Duffy, T. S. (2002). Tetragonal structure of $CaSiO_3$ perovskite above 20 GPa: Structure of $CaSiO_3$ perovskite. *Geophysical Research Letters*, *29*(24), 19-1–19-4. https://doi.org/10.1029/2002GL016148

Smith, J. S., Isayev, O., & Roitberg, A. E. (2017). ANI-1: An extensible neural network potential with DFT accuracy at force field computational cost. *Chemical Science*, *8*(4), 3192–3203. https://doi.org/10.1039/C6SC05720A

Stixrude, L., Cohen, R. E., Yu, R., & Krakauer, H. (1996). Prediction of phase transition in CaSiO3 perovskite and implications for lower mantle structure. *American Mineralogist*, *81*, 1293–1296. https://doi.org/10.2138/am-1996-9-1030

Stixrude, L., Lithgow-Bertelloni, C., Kiefer, B., & Fumagalli, P. (2007). Phase stability and shear softening in CaSiO3 perovskite at high pressure. *Physical Review B: Condensed Matter*, *75*(2), 024108. https://doi.org/10.1103/PhysRevB.75.024108

Sun, N., Mao, Z., Yan, S., Wu, X., Prakapenka, V. B., & Lin, J.-F. (2016). Confirming a pyrolitic lower mantle using self-consistent pressure scales and new constraints on CaSiO3 perovskite. *Journal of Geophysical Research: Solid Earth*, *121*(7), 4876–4894. https://doi.org/10.1002/2016JB013062

Sun, T., Zhang, D.-B., & Wentzcovitch, R. M. (2014). Dynamic stabilization of cubic CaSiO3 perovskite at high temperatures and pressures from ab initio molecular dynamics. *Physical Review B: Condensed Matter*, *89*(9), 094109. https://doi.org/10.1103/PhysRevB.89.094109

Sun, Y., Mendelev, M. I., Zhang, F., Liu, X., Da, B., Wang, C., et al. (2023). *Ab Initio* melting temperatures of bcc and HCP iron under the Earth's inner core condition. *Geophysical Research Letters*, *50*(5), e2022GL102447. https://doi.org/10.1029/2022GL102447

Tadano, T., Gohda, Y., & Tsuneyuki, S. (2014). Anharmonic force constants extracted from first-principles molecular dynamics: Applications to heat transfer simulations. *Journal of Physics: Condensed Matter*, *26*(22), 225402. https://doi.org/10.1088/0953-8984/26/22/225402

Tadano, T., & Tsuneyuki, S. (2015). Self-consistent phonon calculations of lattice dynamical properties in cubic SrTiO3 with first-principles anharmonic force constants. *Physical Review B: Condensed Matter*, *92*(5), 054301. https://doi.org/10.1103/PhysRevB.92.054301

Tang, L., Zhang, C., Sun, Y., Ho, K.-M., Wentzcovitch, R. M., & Wang, C.-Z. (2023). Structure and dynamics of Fe90Si3O7 liquids close to Earth's liquid core conditions. *Physical Review B: Condensed Matter*, *108*(6), 064104. https://doi.org/10.1103/PhysRevB.108.064104

Thompson, A. P., Swiler, L. P., Trott, C. R., Foiles, S. M., & Tucker, G. J. (2015). Spectral neighbor analysis method for automated generation of quantum-accurate interatomic potentials. *Journal of Computational Physics*, *285*, 316–330. https://doi.org/10.1016/j.jcp.2014.12.018

Thomson, A. R., Crichton, W. A., Brodholt, J. P., Wood, I. G., Siersch, N. C., Muir, J. M. R., et al. (2019). Seismic velocities of $CaSiO_3$ perovskite can explain LLSVPs in Earth's lower mantle. *Nature*, *572*(7771), 643–647. https://doi.org/10.1038/s41586-019-1483-x

Togo, A., & Tanaka, I. (2015). First principles phonon calculations in materials science. *Scripta Materials*, *108*, 1–5. https://doi.org/10.1016/j.scriptamat.2015.07.021

Tsuchiya, T., Caracas, R., & Tsuchiya, J. (2004). First principles determination of the phase boundaries of high-pressure polymorphs of silica. *Geophysical Research Letters*, *31*(11), 2004GL019649. https://doi.org/10.1029/2004GL019649

Uchida, T., Wang, Y., Nishiyama, N., Funakoshi, K., Kaneko, H., Nozawa, A., et al. (2009). Non-cubic crystal symmetry of CaSiO3 perovskite up to 18 GPa and 1600 K. *Earth and Planetary Science Letters*, *282*(1–4), 268–274. https://doi.org/10.1016/j.epsl.2009.03.027

Umemoto, K., Kawamura, K., Hirose, K., & Wentzcovitch, R. M. (2016). Post-stishovite transition in hydrous aluminous SiO2. *Physics of the Earth and Planetary Interiors*, *255*, 18–26. https://doi.org/10.1016/j.pepi.2016.03.008

Valencia-Cardona, J. J., Shukla, G., Wu, Z., Houser, C., Yuen, D. A., & Wentzcovitch, R. M. (2017). Influence of the iron spin crossover in ferropericlase on the lower mantle geotherm. *Geophysical Research Letters*, *44*(10), 4863–4871. https://doi.org/10.1002/2017GL073294

Wan, T., Luo, C., Sun, Y., & Wentzcovitch, R. M. (2023). Thermoelastic properties of bridgmanite using deep potential molecular dynamics. https://doi.org/10.48550/arXiv.2307.07127

Wang, W., Xu, Y., Sun, D., Ni, S., Wentzcovitch, R., & Wu, Z. (2020). Velocity and density characteristics of subducted oceanic crust and the origin of lower-mantle heterogeneities. *Nature Communications*, *111*(11), 1–8. https://doi.org/10.1038/s41467-019-13720-2

Wang, X., Wang, Z., Gao, P., Zhang, C., Lv, J., Wang, H., et al. (2023). Data-driven prediction of complex crystal structures of dense lithium. *Nature Communications*, *14*(1), 2924. https://doi.org/10.1038/s41467-023-38650-y

Wang, Y., Weidner, D. J., & Guyot, F. (1996). Thermal equation of state of $CaSiO_3$ perovskite. *Journal of Geophysical Research*, *101*(B1), 661–672. https://doi.org/10.1029/95JB03254

Wu, F. (2024). Figure data. https://doi.org/10.5281/zenodo.10460440

Yang, F., Zeng, Q., Chen, B., Kang, D., Zhang, S., Wu, J., et al. (2022). Lattice thermal conductivity of $MgSiO_3$ perovskite and post-perovskite under lower mantle conditions calculated by deep potential molecular dynamics. *Chinese Physics Letters*, *39*(11), 116301. https://doi.org/10.1088/0256-307X/39/11/116301

Yu, Y. G., Wentzcovitch, R. M., Vinograd, V. L., & Angel, R. J. (2011). Thermodynamic properties of $MgSiO_3$ majorite and phase transitions near 660 km depth in $MgSiO_3$ and Mg_2SiO_4: A first principles study. *Journal of Geophysical Research*, *116*(B2), B02208. https://doi.org/10.1029/2010JB007912

Zhang, C., Tang, L., Sun, Y., Ho, K.-M., Wentzcovitch, R. M., & Wang, C.-Z. (2022). Deep machine learning potential for atomistic simulation of Fe-Si-O systems under Earth's outer core conditions. *Physical Review Materials*, *6*, 063802. https://doi.org/10.1103/PhysRevMaterials.6.063802

Zhang, D.-B., Sun, T., & Wentzcovitch, R. M. (2014). Phonon Quasiparticles and Anharmonic free energy in complex systems. *Physical Review Letters*, *112*(5), 058501. https://doi.org/10.1103/PhysRevLett.112.058501

Zhang, L., Han, J., Wang, H., Car, R., & E, W. (2018). Deep potential molecular dynamics: A scalable model with the accuracy of quantum mechanics. *Physical Review Letters*, *120*(14), 143001. https://doi.org/10.1103/PhysRevLett.120.143001

Zhang, L., Han, J., Wang, H., Saidi, W. A., Car, R., & E, W. (2018). End-to-end symmetry preserving inter-atomic potential energy model for finite and extended systems. https://doi.org/10.48550/arXiv.1805.09003

Zhang, L., Wang, H., Car, R., & E, W. (2021). Phase diagram of a deep potential water model. *Physical Review Letters*, *126*(23), 236001. https://doi.org/10.1103/PhysRevLett.126.236001

Zhang, Z., Irving, J. C. E., Simons, F. J., & Alkhalifah, T. (2023). Seismic evidence for a 1000 km mantle discontinuity under the Pacific. *Nature Communications*, *14*(1), 1714. https://doi.org/10.1038/s41467-023-37067-x

Zhang, Z., & Wentzcovitch, R. M. (2021). *Ab initio* anharmonic thermodynamic properties of cubic CaSiO3 perovskite. *Physical Review B: Condensed Matter*, *103*(10), 104108. https://doi.org/10.1103/PhysRevB.103.104108

Zhang, Z., Zhang, D.-B., Sun, T., & Wentzcovitch, R. M. (2019). phq: A Fortran code to compute phonon quasiparticle properties and dispersions. *Computer Physics Communications*, *243*, 110–120. https://doi.org/10.1016/j.cpc.2019.05.003

References From the Supporting Information

Doyle, A. E., Young, E. D., Klein, B., Zuckerman, B., & Schlichting, H. E. (2019). Oxygen fugacities of extrasolar rocks: Evidence for an Earth-like geochemistry of exoplanets. *Science*, *366*(6463), 356–359. https://doi.org/10.1126/science.aax3901

Kingma, D. P., & Ba, J. (2014). Adam: A method for stochastic optimization. arXiv Prepr. arXiv:1412.6980. https://doi.org/10.48550/arXiv.1412.6980

Martyna, G. J., Klein, M. L., & Tuckerman, M. (1992). Nosé–Hoover chains: The canonical ensemble via continuous dynamics. *Journal of Chemical Physics*, *97*(4), 2635–2643. https://doi.org/10.1063/1.463940

Vandermause, J., Torrisi, S. B., Batzner, S., Xie, Y., Sun, L., Kolpak, A. M., & Kozinsky, B. (2020). On-the-fly active learning of interpretable Bayesian force fields for atomistic rare events. *Npj Computational Materials*, *6*(1), 20. https://doi.org/10.1038/s41524-020-0283-z

Wen, T., Zhang, L., Wang, H., E, W., & Srolovitz, D. J. (2022). Deep potentials for materials science. *Materials Futures*, *1*(2), 022601. https://doi.org/10.1088/2752-5724/ac681d